

Abstract

Quantum Error Correction is an essential ingredient for scaling up a quantum computer. The Nitrogen-Vacancy (NV) center in diamond is a promising candidate for such a scalable quantum computer. This thesis will first explain the basic tools available to control the NV-center and strongly coupled spins in its environment. We will then demonstrate how the spin register can be extended by addressing weakly coupled carbon-spins. The main result of this thesis is the creation of entanglement of these weakly coupled spins, for which initialization, control and read-out is required. We demonstrate entanglement with a fidelity of $F = 0.76 \pm 0.02$, well above the quantum limit for an entangled state. The last chapter will provide an outlook on how the capabilities developed can be used to implement QEC.

Contents

1	Introduction	5
1.1	Quantum Computing	5
1.2	Quantum Error Correction	5
1.3	Weakly coupled carbons; a naturally occurring register	5
2	The Nitrogen-Vacancy center in Diamond	7
2.1	The electronic spin	7
2.1.1	Initialization and readout of the electronic-spin state	7
2.1.2	Controlling the electronic-spin state	8
2.2	Controlling nuclear spins	8
2.2.1	The Hyperfine Interaction	8
2.2.2	Controlling the nitrogen nuclear spin	9
2.2.3	Strongly coupled spins	10
2.3	Decoherence	10
2.3.1	Decoherence time	10
2.3.2	Relation between decoherence and transition broadening	10
3	Addressing Weakly-coupled Carbon Spins	13
3.1	Extending Electron Coherence	13
3.1.1	Spin-Echo	14
3.1.2	Dynamical Decoupling	14
3.1.3	Dynamical decoupling spectroscopy	14
3.2	Identifying weakly-coupled carbon-pins	15
3.2.1	The effect of dynamical decoupling on weakly coupled nuclear spins	15
3.2.2	Identifying Individual Carbon-spins	17
3.3	Characterizing weakly-coupled carbon spins	17
3.3.1	Basic operations	17
3.3.2	Carbon Ramsey experiment	18
4	Controlling Weakly-coupled Carbon Spins	21
4.1	Initialization and readout of single spins	21
4.2	The parity measurement	22
4.3	Quantum state tomography	23
4.3.1	Readout	23
4.3.2	Initialization and tomography of multiple weakly coupled spins	23
4.4	Demonstrating entanglement between weakly coupled carbons	23
5	Outlook: towards Quantum Error Correction	27
5.1	Direct outlook, deterministic operations/what needs to be done/can be done	27
5.2	Simulations, how many carbon can we control?	27
5.2.1	Effect of the magnetic field	27

A	Dynamical Decoupling Spectroscopy	31
A.1	Mathematical description of dynamical decoupling spectroscopy	31
A.2	Fingerprint analysis	31
B	Constants and Experimental values	33

1

Introduction

An essential feature for a scalable quantum computer is the ability to correct for quantum errors. The Nitrogen-Vacancy center in diamond is a promising candidate for a scalable quantum computer. In order to perform

This chapter will explain why building a quantum computer is cool/important/essential/someotherbigword Explain why quantum error correction is essential in achieving this goal Requirements to perform quantum error correction Explain NV natural candidate Requirements 3-5 qubits + entanglement. This thesis will demonstrate how to address weakly coupled carbon spins and create entanglement between them.

1.1 Quantum Computing

The idea of using a quantum mechanical system to simulate physics was first explored by Feynman[7]. Because the Hilbert space(/state space?) of a quantum mechanical system scales exponentially with it's size one would need an exponentially large classical computer to simulate it's behavior. By manipulating a quantum mechanical system directly this scaling problem can be circumvented.

It was quantum simulation that eventually led to the idea of exploiting quantum effects to perform more efficient calculations but it wasn't until Shor's discovery of a remarkably efficient quantum algorithm for prime factorization in 1994[13] that quantum information science really took off.

Shor's algorithm was the first example where a quantum computer can provide an exponential speedup over a classical computer. Shor's and other quantum algorithms allow solving classes of problems that were previously unsolvable, a well known example being the breaking of classical encryption codes.

By now Shor's algorithm has been shown to work on a range of different small scale quantum computers [19] [Needs reference to Shor in different systems or basic algorithms in range of systems] but making a scalable quantum computer that can take full advantage of the exponential speedup proves elusive.

1.2 Quantum Error Correction

1.3 Weakly coupled carbons; a naturally occurring register

The Nitrogen Vacancy centre in diamond is a well investigated system[6] and a promising candidate for quantum computation[3]. In order to implement three qubit measurement based QEC we need three qubits plus ancillae that we can initialise, measure and conditionally perform operations on. These extra qubits are found in Carbon-13 atoms, which are normally a source of decoherence. These atoms can be addressed using a resonant decoupling sequence[15].

2

The Nitrogen-Vacancy center in Diamond

The Nitrogen-Vacancy (NV) center in diamond provides a natural occurring qubit register in a solid state environment. This chapter will explain how the electronic and nuclear spins can be initialized, controlled and read-out using optical and microwave pulses. The methods described in this chapter are limited to spins for which transitions can be addressed selectively. The control of other spins is limited by decoherence.

2.1 The electronic spin

The NV-center is a naturally occurring impurity in diamond consisting of a substitutional nitrogen and an adjacent lattice vacancy (Fig. 2.1a). The NV-center can be in a neutral charge state (NV^0) and a negatively charged state (NV^-). In this thesis we are mainly interested in the negatively charged state, where an additional electron is captured from the environment. In the NV^- state a spin-triplet is formed in the band gap by two electrons. This forms the basis of our qubit.

The electronic ground state can be described by the Hamiltonian [2]:

$$H_{\text{GS}} = \Delta S_z^2 + \gamma_e \mathbf{B} \cdot \mathbf{S} \quad (2.1)$$

Where \mathbf{S}_i are the Pauli-spin operators, $\gamma_e = 2.802 \text{ MHz/G}$ the gyro-magnetic ratio and $\Delta \approx 2.88\text{GHz}$ the zero-field splitting. In this expression the interactions with the nitrogen nucleus and the carbon spin bath are not included. In the experiments a magnetic field $B_z = 304\text{G}$ is applied along the NV-axis¹. The magnetic field lifts the degeneracy of the $m_s = \pm 1$ states through the Zeeman effect.

We define our electronic qubit as the two level system $m_s = 0 := |0\rangle$ and $m_s = +1 := |1\rangle$.

2.1.1 Initialization and readout of the electronic-spin state

The transitions between the electronic ground-state and excited state are spin dependent and lie in the optical domain (637 nm). At low temperatures these transitions can be resonantly excited using a laser of the corresponding frequency. For this reason, experiments were performed at cryogenic temperatures (4K). The frequencies of these transitions depend on magnetic field and strain [10].

Figure 2.1b shows the optical transitions used to initialize and read-out the electronic spin. The A_1 transition excites both the $m_s = +1$ and the $m_s = -1$ states to the excited state. The E_x transition excites the $m_s = 0$ state to the excited state. When the spin falls back to the ground state there is a small probability that the spin is flipped, denoted by the dashed line.

The spin can be initialized by pumping one of these transitions[12]. This will cause the population to cycle between the ground and excited state with a small probability of the spin flipping. When the spin flips it ends up in the state that is not being addressed and stays there.

The optical transitions can also be used to read-out the spin state. By applying a pulse to the E_x transition a photon can be detected when the state falls back to the ground state. Because the E_x only excites the $m_s = 0$ state photons can only be detected when the system is in the $|0\rangle$ -state. By keeping the pulse short the probability that the spin flips is kept low.

¹The NV-axis is the axis going through both the nitrogen and the vacancy.

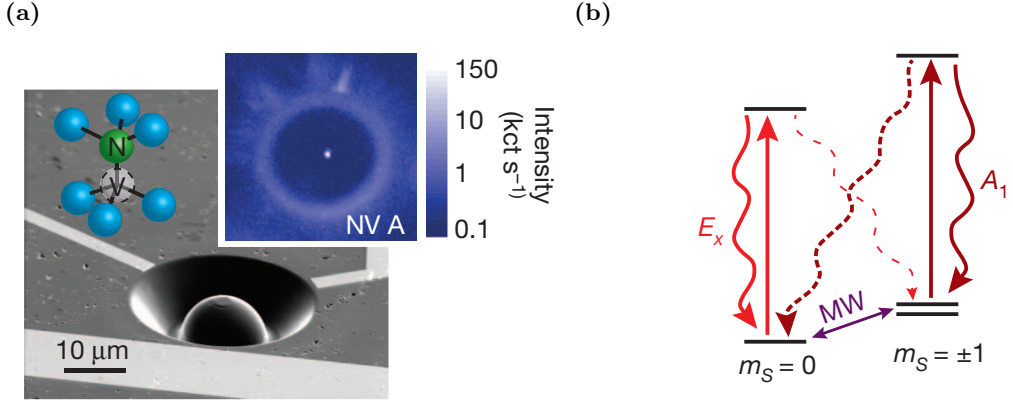


Figure 2.1 – Figure 2.1a, Scanning electron microscope image of a solid immersion lens (SIL) similar to those used in the experiments. Overlaid sketch shows a schematic representation of the NV-center. Inset shows a scanning confocal microscope of an NV-center similar to those used in the experiments. Figure from [12]. Figure 2.1b, Energy levels used for initialization and readout of the electronic-spin state. Figure from [12]

Because the number of pumping cycles before the spin flips is limited the fidelity with which the spin can be read-out is limited by how well the few photons that are emitted are detected. A solid immersion lens (SIL), visible in Fig. 2.1a, is milled onto the sample to maximize the detection efficiency.

Using these methods the experiments were performed at a readout fidelity $F = 90.55 \pm 0.40\%$.

2.1.2 Controlling the electronic-spin state

The state of a qubit can be represented as a vector on the Bloch-sphere where the $|0\rangle$ -state lies at the north pole and the $|1\rangle$ -state at the south pole. On the Bloch-sphere the state vector rotates around the quantization-axis with a frequency depending on the energy splitting between the two states: the Larmor frequency. For the NV-electronic spin the Larmor frequency is given by Eq. (2.2) and the quantization axis points in the z-direction (towards $|0\rangle$).

$$\omega_L = \Delta + \gamma_e B_z \quad (2.2)$$

By applying an external field a term is added to the Hamiltonian, changing the quantization-axis and thereby its evolution. By applying microwaves with a frequency equal to ω_L the transition between $|0\rangle$ and $|1\rangle$ can be driven [11]. Resonant microwave pulses are applied to the sample through on-chip lead, visible in Fig. 2.1a as the light area just below the SIL.

2.2 Controlling nuclear spins

The electronic-spin interacts with nuclear spins in its environment through the hyperfine interaction. Close-by spins have a strong hyperfine interaction and can be controlled directly by applying microwave pulses. When the interaction is too weak the spins cannot be readily resolved and are a source of decoherence.

2.2.1 The Hyperfine Interaction

The coupling between the electronic spin of the NV-center and a nuclear-spin is given by the hyperfine-interaction. The hyperfine-interaction is a spin dependent interaction that is not present for spin-0 particles such as carbon-12.

For nuclear spins the Hamiltonian depends on the electronic spin-state of the NV-center. For a magnetic field (B_z) in the z-direction the Hamiltonian is given by Eq. (2.3) when the electronic-spin is in the $m_s = 0$ state, and by Eq. (2.4) when in the $m_s = +1$ state[17]. Where \mathbf{I} and \mathbf{S} are the nuclear and electronic spin operators, γ_n is the gyro-magnetic ratio of the nucleus and $Q = 2\pi \cdot 4.946\text{MHz}$ [2] is the nuclear quadrupole splitting of the nitrogen. The quadrupole term is not present when the nuclear spin is not a Nitrogen.

$$H_0 = -Q\mathbf{I}_z^2 + \gamma_n B_z I_z \quad (2.3)$$

$$H_1 = -Q\mathbf{I}_z^2 + \gamma_n B_z I_z + H_{\text{HF}} \quad (2.4)$$

The Larmor frequency for a nucleus is given by Eq. (2.5).

$$\omega_L = -Q\mathbf{I}_z^2 + \gamma_n B_z \cdot \hat{\mathbf{z}} \quad (2.5)$$

The hyperfine (H_{HF}) term consists of a contact term and a dipole term. The contact term results from an overlap between the electronic- and nuclear- wave-functions. The contact term is negligible for all but the nuclear-spins closest to the NV-center. For close-by carbon spins hyperfine couplings have been calculated [8, 9] and measured [14].

The dipole term is given by Eq. (2.6) [4] Where \mathbf{n}_{HF} is a unit vector pointing from the electronic spin to the nucleus, r is the distance between the electronic and nuclear spin, and μ_0 the magnetic constant. The dipole term can be split into a parallel and orthogonal component such that $H_{\text{HF}} = A_{\parallel} I_z + A_{\perp} I_x$ when the contact term is negligible.

$$H_{\text{dip}} = \frac{\mu_0 \gamma_e \gamma_C \hbar^2}{4\pi r^3} [\mathbf{S} \cdot \mathbf{I} - 3(\mathbf{S} \cdot \mathbf{n}_{\text{HF}})(\mathbf{I} \cdot \mathbf{n}_{\text{HF}})] \quad (2.6)$$

From Eq. (2.6) the parallel and orthogonal components of the hyperfine interaction, with respect to the NV-axis along the z-direction, can be derived to be:

$$A_{\parallel} = -\frac{\mu_0 \gamma_e \gamma_C \hbar^2}{4\pi r^3} \left(3 \cdot \frac{z^2}{r^2} - 1 \right) \quad (2.7)$$

$$A_{\perp} = -\frac{\mu_0 \gamma_e \gamma_C \hbar^2}{4\pi r^3} \left(3 \cdot \frac{\sqrt{x^2 + y^2} \cdot z}{r^2} \right) \quad (2.8)$$

2.2.2 Controlling the nitrogen nuclear spin

The nitrogen-spin adjacent to the vacancy can be controlled using the spin-dependent hyperfine interaction. Because both the zero-field splitting Δ of the electronic-spin and the nuclear quadrupole splitting Q are much larger than the hyperfine coupling between the nuclear and electronic spin ($A_N = 2\pi \cdot 2.186$ MHz), the secular approximation can be used, leading to the following system Hamiltonian:

$$H_{\text{GS}} = \Delta S_z^2 + \gamma_e \mathbf{B} \cdot \mathbf{S} - Q\mathbf{I}_z^2 + \gamma_n B_z I_z - A_N \mathbf{S}_z \cdot \mathbf{I}_z \quad (2.9)$$

The hyperfine interaction between the nitrogen and electronic spin causes the transition between $m_s = 0$ and $m_s = 1$ to be split. This magnitude of the splitting is equal to A_N and is clearly visible in the Electron Spin Resonance (ESR) showed in the top panel of Fig. 2.2.

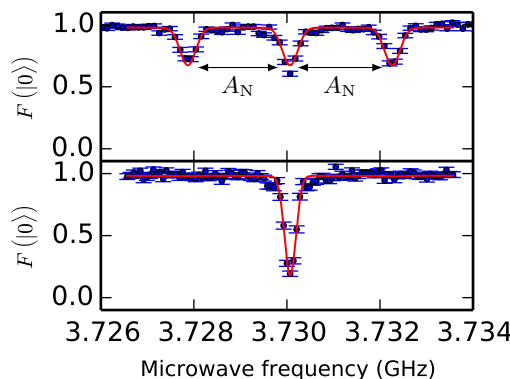


Figure 2.2 – Electron Spin Resonance (ESR) for uninitialized (top) and initialized nitrogen spin (bottom) of the $m_s = 0 \rightarrow m_s = +1$ transition. In a dark ESR the spin is prepared in $|0\rangle$, a microwave pulse is applied and then the $|0\rangle$ state is read-out again. This is done for a range of frequencies. When the microwave is on resonance with a transition the spin will be rotated and a dip will be visible in the signal. In the top figure the transition is split due to the interaction with the nearby nitrogen atom. In the lower figure the nitrogen state is initialized and the splitting disappears.

Because the interaction is spin-dependent it can be used to measure the nitrogen's spin state. Every time an experiment is started the nitrogen starts out in a mixed state. This means that every time an uninitialized nitrogen is measured it is equally likely to end up in one of its three

states. The nitrogen state can be measured by initializing the electron in the split $m_s = +1$ state and driving one of the transitions to $m_s = 0$. Only if the nitrogen was in the state corresponding to the transition being driven will a measurement of the $m_s = 0$ state give a positive result.

By resetting and repeating this procedure until a positive result is measured the nitrogen-spin can be initialized. The system can be reset into a mixed state by applying a high-energy off-resonant laser pulse. This procedure is known as Measurement Based Initialization (MBI) and is used in our experiments. The lower panel of Fig. 2.2 shows an ESR after the nitrogen has been initialized using MBI.

2.2.3 Strongly coupled spins

The ability to control spin states relies on being able to selectively address its spin dependent transitions. When two transitions can be resolved in an ESR they can be addressed by applying microwave pulses of the corresponding frequencies. However if two transitions overlap in an ESR, applying a microwave pulse at the corresponding frequency will address both transitions and it is not possible to control its spin state.

Two transitions cannot be resolved when the splitting between them is smaller than the width of the transition. The magnitude of the splitting is determined by the strength of the interaction and the broadening of the transitions is caused by decoherence. We define a spin to be strongly coupled when it is possible to readily resolve its transitions in an ESR experiment with negligible power broadening. Conversely a spin is weakly coupled when it is not possible to readily resolve its transitions in an ESR.

Strongly coupled spins can be controlled by applying microwaves directly at the transition frequency, weakly coupled spins can not. Using this method strongly-coupled carbon-13 spins have been controlled and initialized[12].

2.3 Decoherence

The ESR signal is broadened because the NV-center interacts with an environment known as the spin bath. The spin bath consists of a very large number of spins that are all very weakly coupled to the NV-center. Just like the uninitialized nitrogen spin these are in a mixed state. This means that for every iteration of an experiment the spin bath can have a different configuration. These different configurations of the spin bath slightly shift the addressed transition around causing the broadening of the transition.

2.3.1 Decoherence time

These variations in the spin-bath configuration can be measured with a Ramsey experiment. In a Ramsey experiment (Fig. 2.3a) the electronic spin is brought into a superposition between the $|0\rangle$ and $|1\rangle$ -state where it freely evolves for a time τ . A final pulse brings the state back into $|0\rangle$ where it is read out.

By applying a slight detuning to the rotating frame used to keep the phase fixed an oscillation can be seen in the signal (Fig. 2.3b). Due to the different spin-bath configurations the evolution frequency varies slightly between experiments, this causes the measured signal to decay as the different oscillations move out of phase with each other. The decay is known as decoherence and the $1/e$ -time of the decay is known as the decoherence time.

For a Ramsey experiment the decay follows a Gaussian profile Eq. (2.10). T_2^* is defined as the $1/e$ time of the decay as measured by a Ramsey experiment. The T_2^* of our sample was measured to be $T_{2,e}^* = 4.54 \pm 14\mu\text{s}$ with initialized nitrogen-spin. The decay follows a Gaussian profile within two σ : $n = 1.81 \pm 0.14$

$$K(\tau) = e^{-(\frac{\tau}{T_{2e}^*})^2} \quad (2.10)$$

2.3.2 Relation between decoherence and transition broadening

The decay in a Ramsey experiment is a measure for variations of the spin-bath in the time-domain while the broadening of transitions in an ESR is a measure for variations of the spin-bath in the frequency domain. The decay of the Ramsey and the shape of the ESR are related through a Fourier

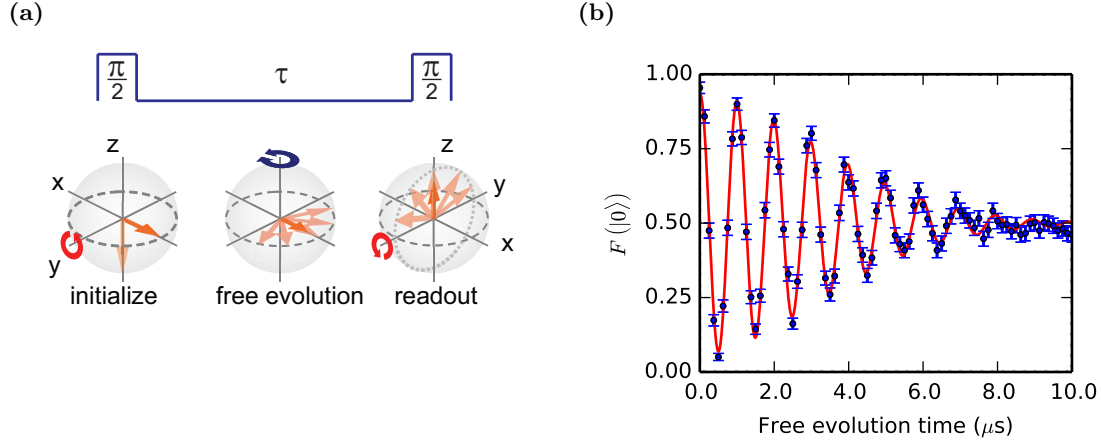


Figure 2.3 – Figure 2.3a, schematic representation of a Ramsey experiment. Figure from de Lange [4]. In a Ramsey experiment a qubit is brought into the xy -plane by a $\pi/2$ -pulse where it evolves freely for a time τ before being subjected to a final $\pi/2$ pulse to read out its x -component. By applying a detuning to the rotating frame the spin will pick up a phase $\phi = \omega_d\tau$ during free evolution. The final pulse will rotate the spin towards the poles depending on the phase picked up during free evolution. This manifests itself as an oscillation. Because the configuration of the spin-bath is slightly different between experiments the frequency of the oscillation will vary with each iteration. This variation in frequency between iterations will cause the oscillation to decay. Figure 2.3b shows a Ramsey experiment for the electronic spin. A T_{2e}^* of $4.54 \pm 0.14 \mu\text{s}$ was measured for the electronic spin. The decay follows a Gaussian profile within uncertainty $n = 1.81 \pm 0.14$.

transform and described by Eq. (2.11)². Where C is a constant that depends on the duration and power of the ESR microwave pulse. Because the decay of the Ramsey is Gaussian the shape of a transition in the ESR is also Gaussian.

$$\mathcal{F}\{K(\tau)\} = Ce^{-\frac{(2\pi \cdot f)^2 \cdot T_{2e}^{*2}}{4}} \quad (2.11)$$

Two identical Gaussians can be readily resolved when the separation between their maxima is larger than their full-width-half-maximum (FWHM). The FWHM (in Hz) of the ESR is given by Eq. (2.12).

$$\text{FWHM} = \frac{2\sqrt{\ln 2}}{\pi T_{2e}^{*2}} \quad (2.12)$$

An estimation of when carbon spins can be resolved can be made by looking at the strength of the hyperfine interaction. The splitting caused by a carbon spin is equal to twice the total interaction strength A at low magnetic field ($\gamma_e B \ll A$). At high field ($\gamma_e B \gg A$) the secular approximation is valid and the splitting is twice the parallel component of the hyperfine A_{\parallel} . We can readily resolve a transition when the shift due to the corresponding interaction is larger than the FWHM of the transition.

At a natural concentration of carbon-13 NV-centers have a typical electron $T_{2e}^* \approx 2 \mu\text{s}$ that depends on the exact configuration of the spin-environment. Increasing the carbon-13 concentration generally reduces T_{2e}^* . On the sample used for the experiments $T_{2e}^* = 4.54 \pm 0.14 \mu\text{s}$ was measured. This means that the hyperfine coupling must be larger than $2\pi \cdot 265 \text{ kHz}$ in a typical NV-center, and larger than $2\pi \cdot 117 \text{ kHz}$ in the sample used in this thesis for a carbon to be strongly coupled.

As the presence of strongly coupled carbons close to the NV-center is governed by probability and the probability of getting 3-5 strongly coupled carbons is very low it is necessary to develop methods to address weakly coupled carbons. The next chapter will demonstrate methods to extend the coherence time and address weakly coupled carbons, thereby enlarging the spin-register.

²Assuming negligible power broadening in the ESR, and linear response (How do i explain clearly that in low power regime, not driving all the way through?)

3

Addressing Weakly-coupled Carbon Spins

The spin register can be extended by addressing weakly-coupled spins. This chapter will explain how coherence can be extended through dynamical decoupling and how this can be used to address single carbon-spins. The methods will be used to identify and characterize individual nuclear spins.

[NOTE: Maybe remove following paragraph and figure?]

Figure 3.1 shows a schematic representation of different coupling regimes. Carbons in region II are in the strong coupling regime, transitions of these spins can be readily resolved and they can be controlled using the methods described in the previous chapter. By extending the coherence of the electronic spin certain weakly coupled spins can be controlled [16]. These can be found in region III. Control of spins in region III is not limited by the coherence of the electronic-spin but by that of the nucleus. These spins cannot be addressed without inventing new methods that significantly improve both electronic- and nuclear- spin coherence.

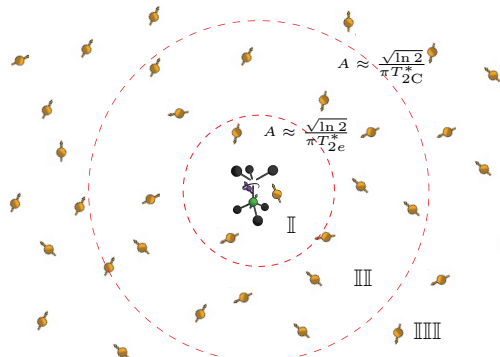


Figure 3.1 – Schematic representation of different coupling regimes. In the strong coupling regime (region II) carbon-spins are coupled to the NV-center stronger than the coupling of the NV-center to the spin-bath. These carbons can be addressed directly. In the weak coupling regime (region III) carbon-spins are coupled more strongly to the NV-center than to the spin-bath but not strong enough to be addressed directly. In the very-weak coupling regime (region IIII) the coupling to the spin-bath is stronger than the coupling to the NV-center. These spins cannot be addressed.

3.1 Extending Electron Coherence

To be able to resolve weakly coupled carbons it is necessary to extend the coherence of the NV-spin. By using a technique known as a spin-echo the effect of variations in the environment *between* experiments can be eliminated, making variations *during* experiments the main source of decoherence. By dynamical decoupling the effect of these variations on the coherence can be minimized and the dynamics of the spin-bath can be exposed.

3.1.1 Spin-Echo

A spin echo experiment (Fig. 3.2) is very similar to a Ramsey experiment. The difference is an additional π pulse that is added in the middle of the experiment exactly between the $\pi/2$ pulses of the Ramsey sequence. In a spin echo the state is brought into the xy -plane where it evolves for a time $\tau/2$ before a π -pulse, along the y -direction in the rotating frame, is applied. It evolves for another $\tau/2$ before a final $\pi/2$ -pulse rotates it back to $|0\rangle$ and it is read out.

The key component of a spin-echo is the central π -pulse that cancels out the effect of quasi-static variations in the spin-bath configuration. The π -pulse can be seen as turning the reference frame of the NV-spin upside down. If the spin-bath configuration does not change during the experiment, the detuning of the evolution frequency with respect to the central frequency during the first part will be exactly opposite to the detuning during the second part. This means that any phase difference picked up during the first half of the evolution is canceled out perfectly during the second half of the evolution.

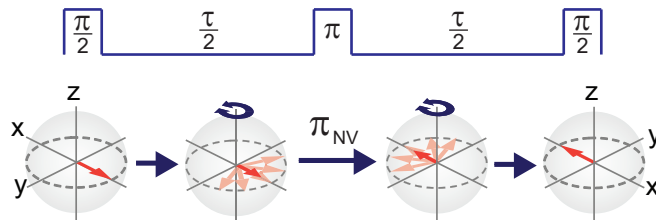


Figure 3.2 – In a spin echo experiment the qubit is brought into the xy -plane of the Bloch-sphere by a $\pi/2$ -pulse. Here it freely evolves for a time $\tau/2$ before being flipped by a π -pulse along the y -axis of the rotating frame. It is let to evolve for another $\tau/2$ before a final $\pi/2$ pulse brings it used to read out the x -component. If the spin-bath configuration does not change during the free evolution time τ the state vector will end up along the x -axis irrespective of the initial spin-bath configuration. Figure from de Lange [4].

Because the spin-bath does not remain static during experiments the cancellation is not perfect, some phase is picked up causing the signal to decohere. Similar to a Ramsey experiment this can be measured by applying a detuning to the rotating frame and measuring the decay of the oscillation. T_2 is defined as the $1/e$ value of the decay of a spin echo experiment and measures decoherence due to variations in the spin-bath during an experiment. T_2 was measured to be $1.10 \pm 0.01\text{ms}$.

3.1.2 Dynamical Decoupling

A natural way to extend the phase cancellation properties of the spin-echo experiment to shorter timescales is by applying more π -pulses. This procedure is known as dynamical-decoupling. Similar to how the spin-echo cancels out phase picked up due to any variations that are quasi-static on the time-scale of the experiment, dynamical-decoupling cancels out phase due to variations on the time-scale of the π -pulses. Dynamical-decoupling can dramatically improve coherence times[5].

On our sample a coherent signal¹ is measured after more than $40\mu\text{s}$ for 256 pulses. Work on ensembles indicates that this can be improved even further by applying more pulses: a coherence time of $T_{DD} \approx 0.6\text{s}$ was reported at 77K [1].

3.1.3 Dynamical decoupling spectroscopy

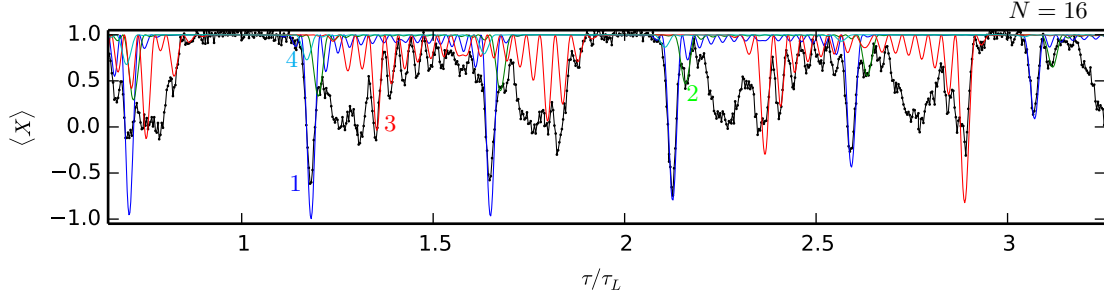
When discussing the Ramsey and the spin-echo experiment we have treated the NV-center as being affected by the spin-bath but not interacting with it. In reality the NV-spin does interact with nuclear spins. It is possible to probe these interactions using a dynamical decoupling spectroscopy. During a dynamical decoupling spectroscopy a fingerprint of the spin environment is constructed.

In a dynamical decoupling spectroscopy experiment the electron is prepared in the $|X\rangle = \frac{1}{\sqrt{2}}(|0\rangle + |1\rangle)$ state. It is subjected to a pulse sequence consisting of $N/2$ blocks of the form $\tau - \pi - 2\tau - \pi - \tau$, where τ is a wait time and π a π -pulse. The experiment is concluded by measuring $\langle X \rangle$. The fingerprint is the result of many repetitions for a range of inter-pulse delays 2τ .

¹ $F|0\rangle > 0.68$

Part of a dynamical decoupling spectroscopy can be seen in Fig. 3.3. When the central spin interacts conditionally with a spin in the environment coherence is lost when the central spin is measured. In a fingerprint such an interaction is visible as a lowered contrast.

(a)



(b)

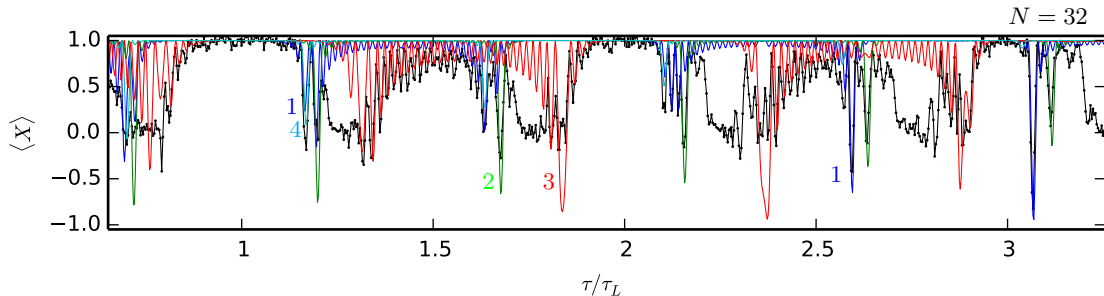


Figure 3.3 – Part of a fingerprint resulting from a dynamical-decoupling-spectroscopy experiment performed at $B_z = 304\text{G}$, $\tau_L = 3.07\mu\text{s}$. Contrast is lowered when the decoupling sequence performs a conditional operation on a spin in the environment. A reference to the full spectroscopy can be found in Appendix A.2. Black lines correspond to data. Colored lines represent computed responses of carbon spins. Responses were calculated using Eq. (A.2) with hyperfine parameters from Table 3.1.

3.2 Identifying weakly-coupled carbon-pins

To be able to control weakly coupled spins the interaction between these spins and the NV-center must be understood. This section will discuss the effect of dynamical decoupling on the interaction between the NV-center and weakly coupled nuclear spins. This knowledge is used to explain the features in the fingerprint of Fig. 3.3 and identify several nuclear spins.

3.2.1 The effect of dynamical decoupling on weakly coupled nuclear spins

During dynamical decoupling the electronic state alternates between the $m_s = 0$ and $m_s = +1$ state, this causes the nuclear spin to alternately rotate around two distinct quantization axes (Fig. 3.4). When the electron is in the $m_s = 0$ state each nuclear spin precesses about ω_L with the Larmor frequency. When the electron is in the $m_s = +1$ state there is a hyperfine interaction between the nucleus and the NV-center (Eq. (2.4)) and the spin precesses around $\tilde{\omega} = \omega_L + \mathbf{A}$, where $\mathbf{A} = A_{\parallel}\hat{\mathbf{z}} + A_{\perp}\hat{\mathbf{x}}$ [16].

The result of a decoupling sequence is a net rotation around an axis $\hat{\mathbf{n}}_i$ by an angle θ . Where $\hat{\mathbf{n}}_i$ depends on the initial state of the electron and θ is proportional to the number of pulses N [16]. $\hat{\mathbf{n}}_i = \hat{\mathbf{n}}_0$ when the electron starts in $m_s = 0$ and $\hat{\mathbf{n}}_i = \hat{\mathbf{n}}_1$ when the electron starts in $m_s = +1$.

When the net rotation axes point in a different direction a conditional operation is executed during dynamical decoupling (Fig. 3.5). In a dynamical decoupling spectroscopy contrast is lost when a conditional operation is executed. To understand when this occurs it is useful to consider three different cases. A weakly coupled carbon spin in: the *trivial* regime where $A_{\perp} = 0$, the *basic* regime where $A_{\perp} \ll \omega_L$ and the *complex* regime where $A_{\perp} \sim \omega_L$. For a complete mathematical

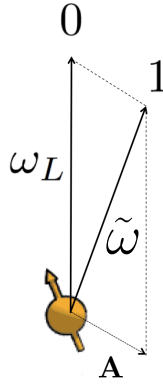


Figure 3.4 – Flipping the electron spin from the $m_s = 0$ to the $m_s = +1$ state changes the quantization axis of nuclear spins. For $m_s = 0$ all nuclear spins precess about ω_L . For $m_s = +1$ each spin precesses about a distinct axis $\tilde{\omega} = \omega_L + \mathbf{A}$.

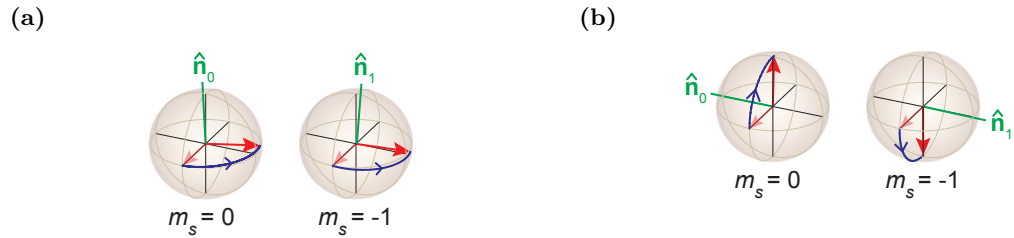


Figure 3.5 – Figure 3.5a When the net rotation axes $\hat{\mathbf{n}}_0$ and $\hat{\mathbf{n}}_1$ point in the same direction the carbon experiences an unconditional rotation and cannot be controlled. Figure 3.5b When the net rotation axes $\hat{\mathbf{n}}_0$ and $\hat{\mathbf{n}}_1$ are anti-parallel the carbon experiences a conditional rotation, either around $+x$ or $-x$, and can be controlled. Figure from [16].

description of the response of nuclear spins to a dynamical decoupling spectroscopy the reader is referred to Appendix A.1.

The trivial regime ($A_{\perp} = 0$)

Because there is no orthogonal component of the hyperfine the spin will precess around the z -axis independent of the initial electronic spin-state. Therefore no conditional operation is possible and it is not possible to resolve such a spin in a dynamical decoupling spectroscopy.

The basic regime ($A_{\perp} \ll \omega_L$)

In the basic regime the net rotation axes are practically parallel and point in the z -direction for almost every τ except for a specific resonant condition for which the axes are anti-parallel. This resonant condition is given by Eq. (3.1), where k is an integer, and has a Lorentzian shape in a dynamical decoupling spectroscopy. The FWHM of the resonance is given by Eq. (3.2).

$$\tau = \frac{(2k+1)\pi}{2\omega_L + A_{\parallel}} \quad (3.1)$$

$$\text{FWHM}_{\text{DD}} = \frac{A_{\perp}}{2\omega_L^2} \quad (3.2)$$

The complex regime ($A_{\perp} \sim \omega_L$)

In the case where ω_L and A_{\perp} are of comparable magnitude the net rotation axes $\hat{\mathbf{n}}_i$ are strongly dependent on the initial electron-state for almost any τ . When a carbon is in the complex regime it is no longer possible to describe it as a narrow resonance in the dynamical decoupling spectroscopy. The response is visible as a wide resonance with an oscillation on top of it.

Because the electron is not interacting with a single carbon but with a bath of carbon atoms the contrast M is given by the product of all individual values M_j for each individual spin j (Eq. (3.3)). When the responses of multiple carbons overlap contrast is quickly lost.

$$M = \prod_j M_j \quad (3.3)$$

In order to distinguish an individual carbon-spin its response must not overlap with that of other carbon spins. By sweeping the number of π -pulses the response of an individual carbon can be distinguished from the response of multiple spins. Only when an individual spin is being addressed is it possible to sweep the contrast of the dynamical decoupling spectroscopy to -1 by increasing the number of pulses.

3.2.2 Identifying Individual Carbon-spins

Going back to Fig. 3.3 it is now possible to explain its features.

A broad feature with low coherence is clearly visible around $\tau/(4\tau_L) = m$ for odd m . This feature is known as the spin-bath collapse and is caused by the response of multiple spins overlapping.

At the edges of the spin bath several sharp dips are visible. These most likely correspond to individual spins. A first estimate of the hyperfine coupling to these spins can be made based on their location and width using Eqs. (3.1) and (3.2).

Between the spin-bath collapses there alternately appears an oscillation. This oscillation is most likely caused by a spin in the complex regime. Its position can be used to get a rough estimate for its hyperfine coupling.

By computing the responses for these estimated hyperfine parameters using Eq. (A.2) a more accurate estimation can be made. The parameters are varied until the computed response agrees with the data as well as possible. Using this method 13 distinct carbon spins were identified.

The parameters of the 4 strongest coupled carbons are listed in Table 3.1 and their computed responses are visible as colored lines in Fig. 3.3. All estimated hyperfine parameters and a link to the full fingerprint measurements can be found in Appendix A.2.

Carbon	A_{\parallel}	A_{\perp}
1	$2\pi \cdot 30.0$ kHz	$2\pi \cdot 80.0$ kHz
2	$2\pi \cdot 27.0$ kHz	$2\pi \cdot 28.5$ kHz
3	$2\pi \cdot -51.0$ kHz	$2\pi \cdot 105.0$ kHz
4	$2\pi \cdot 45.1$ kHz	$2\pi \cdot 20.0$ kHz

Table 3.1 – Estimated hyperfine parameters for spins 1 to 4 in Fig. 3.3.

3.3 Characterizing weakly-coupled carbon spins

Using the knowledge about the interaction between the NV-center and individual nuclear spins it is possible to implement basic gates and characterize the spins. This section will explain how basic gates can be implemented and use these gates to measure the precession frequency and T_2^* of individual carbon spins.

3.3.1 Basic operations

In order to implement basic gates on a nuclear spin we make use of the conditional rotation that occurs on the resonance given by Eq. (3.1). At the resonant condition the nuclear spin rotates about one of two anti-parallel axes depending on the electronic-spin state. The angle of the rotation is proportional to N .

It is possible to calibrate the angle of rotation by bringing the electronic-spin in a superposition, sweeping N and measuring the contrast. If the contrast is swept to -1 an unconditional π -pulse is implemented, being able to sweep the contrast to -1 means the spin is controllable.

By choosing N at 0 contrast on such a spin a conditional $\pi/2$ rotation is implemented. The rotation rotates in the clockwise direction when the electron is in the $|0\rangle$ -state and in the counter-clockwise direction when it is in the $|1\rangle$ -state. We define the axis of rotation of this operation as the x -axis and call the operation the $\pm x$ -gate.

The $\pm x$ -gate forms the basis of our control over weakly coupled spins. Figure 3.6 shows how the $\pm x$ -gate is depicted in a circuit-diagram. An unconditional gate can be implemented by placing the electron in an eigenstate before performing the $\pm x$ -operation. Van der Sar et al. [18] have demonstrated how to integrate regular operations on the NV-spin with a decoupling sequence. By letting the phase of the carbon evolve we are able to apply operations on the carbon-spin with arbitrary phase.

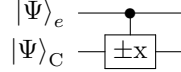


Figure 3.6 – The $\pm x$ -gate performs an x -rotation on the carbon ($|\Psi\rangle_C$) when the electron is in the $|0\rangle_e$ -state. It performs a $-x$ rotation when the electron is in the $|1\rangle_e$ -state.

The $\pm x$ -gate has been calibrated for several spins. The parameters used to implement $\pm x$ -gates are listed in Table 3.2. Carbon-1 and carbon-4 were found to perform the best $\pm x$ -gates.

Carbon	N	τ	total gate time
1	18	9.420 μs	339 μs
2	26	6.620 μs	344 μs
3	14	18.564 μs	520 μs
4	40	6.456 μs	516 μs

Table 3.2 – Parameters used to implement $\pm x$ -gates.

3.3.2 Carbon Ramsey experiment

By performing a Ramsey experiment the precession and dephasing-time T_2^* can be determined. By determining the precession frequencies it is possible to track phase evolution and use it to implement operations with arbitrary phase. By measuring the precession frequency it is also possible to disprove our estimation for the hyperfine parameters. The dephasing time must be measured to determine if it is long enough to implement the gates required for QEC.

In an ordinary Ramsey experiment a qubit is brought to the equator of the Bloch-sphere where it precesses for a time τ before it is read out along the x -direction. A carbon-Ramsey experiment is similar but slightly more complicated as the nuclear spin cannot be controlled and read-out directly.

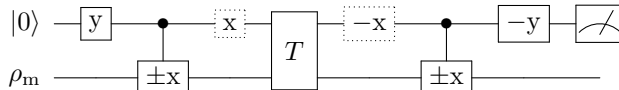


Figure 3.7 – Gate circuit depicting an uninitialized carbon Ramsey. T is the free evolution time. x and y are $\pi/2$ pulses along the x and y axis respectively. The dotted gates are not present when the electron is protected against decoherence by dynamical decoupling during the free evolution time T .

A gate circuit of the uninitialized carbon-Ramsey experiment is depicted in Fig. 3.7. The first pulse brings the electronic spin in the $|X\rangle$ -state. Because the carbon starts out in a mixed state the two-qubit system can be described by the tensor product of two density matrices:

$$\rho_X \otimes \rho_m = \rho_X \otimes \rho_X + \rho_X \otimes \rho_{-X} \quad (3.4)$$

By applying the $\pm x$ -gate the electronic-spin picks up a phase depending on the nuclear spin-state:

$$\rho_Y \otimes \rho_X + \rho_{-Y} \otimes \rho_{-X} \quad (3.5)$$

In this state it is either left to freely evolve for a time T while the electronic spin is protected against decoherence through dynamical decoupling, or a $\pi/2$ -pulse is applied to bring the electron back to the poles of the bloch sphere. If the extra $\pi/2$ -pulse is applied the system is in the following state before the free evolution.

$$\rho_0 \otimes \rho_X + \rho_1 \otimes \rho_{-X} \quad (3.6)$$

Because the electronic spin is in a different state for ρ_X and ρ_{-X} they evolve with different frequencies. After the free evolution another $\pi/2$ -pulse is applied to bring the electronic spin back into the xy -plane.

The final part of the circuit reads out the nuclear spin along the x -direction for $|Y\rangle_e$ and along the $-x$ -direction for $|-Y\rangle_e$. The phase picked up during free evolution show up as an oscillation between $|0\rangle_e$ and $|1\rangle_e$ in the readout.

Determining the precession frequency

Because the uninitialized carbon-Ramsey evolves with two frequencies we expect the measured oscillation to be the sum of two cosines as described by Eq. (3.7). Where $\tilde{\omega} = \sqrt{(\omega_L + A_{\parallel})^2 + A_{\perp}^2}$.

$$\frac{1}{4} \cos(\omega_L \tau) + \frac{1}{4} \cos(\tilde{\omega} \tau) + \frac{1}{2} \quad (3.7)$$

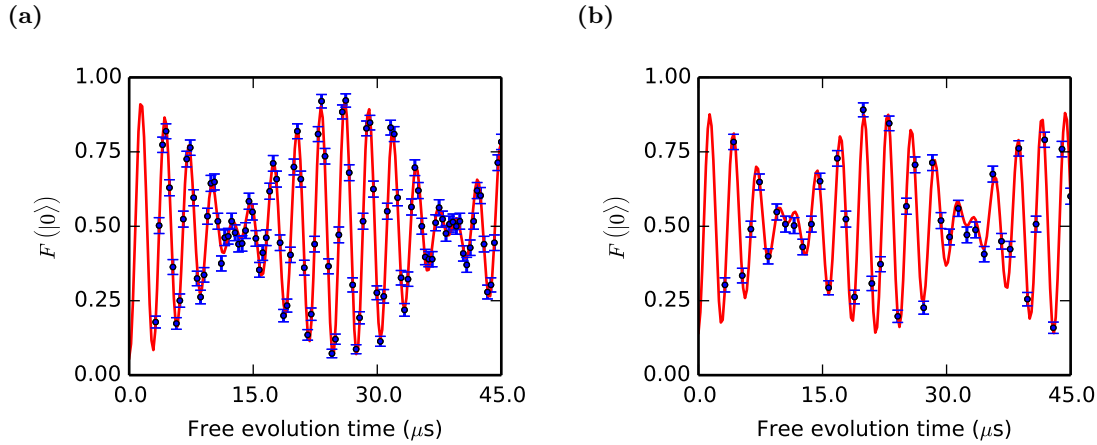


Figure 3.8 – The uninitialized carbon-Ramsey experiment shows an oscillation due to the phase picked up during free evolution. Figure 3.8a shows data for carbon-1 and Figure 3.8b for carbon-4. The measured frequencies were, for carbon-1: $\omega_{L,C1} = 2\pi \cdot 325.81 \pm 0.25$ and $\tilde{\omega}_{C1} = 2\pi \cdot 364.41 \pm 0.23$, and for carbon-4: $\omega_{L,C4} = 2\pi \cdot 325.94 \pm 0.40$ and $\tilde{\omega}_{C4} = 2\pi \cdot 371.52 \pm 0.39$.

Figure 3.8 shows the results for an uninitialized carbon-Ramsey experiment. The data was fitted to a sum of two cosines in order to determine the frequencies.

The Larmor frequencies measured are $\omega_{L,C1} = 2\pi \cdot 325.81 \pm 0.25$ kHz for carbon-1 and $\omega_{L,C4} = 2\pi \cdot 325.94 \pm 0.40$ kHz for carbon-4. Both the measured Larmor frequencies agree with the magnetic field of 304G within two standard deviations.

The $\tilde{\omega}$ frequency can be used to disprove the estimations for the hyperfine parameters listed in Table 3.1, however if the measured values agree with the hyperfine estimation we cannot conclude that the estimations are correct.

Based on the estimated hyperfine parameters we expect $\tilde{\omega}_{C1} \approx 2\pi \cdot 364.7$ kHz for carbon-1 and $\tilde{\omega}_{C4} \approx 2\pi \cdot 371.4$ kHz for carbon-4. For carbon-1 $\tilde{\omega}_{C1} = 2\pi \cdot 364.41 \pm 0.23$ kHz was measured and for carbon-4 $\tilde{\omega}_{C4} = 2\pi \cdot 371.52 \pm 0.39$ kHz was measured. Both these values are in good agreement with experiment, an indication that our hyperfine estimation is accurate.

Measuring $T_{2,C}^*$

To determine $T_{2,C}^*$ for normal operation an uninitialized carbon-Ramsey was performed where the electron was dynamically-decoupled during the free evolution time. Because the electron is constantly flipped the carbon will precess with an average frequency of $\omega_{DD} = (\omega_L + \tilde{\omega})/2$. By undersampling with a frequency slightly detuned from the precession frequency (ω_{DD}) a decaying cosine can be observed where the 1/e time of the envelope is equal to T_2^* .²

Figure 3.9 shows the decay for both carbons. The decay follows a Gaussian profile within uncertainty for both spins. The coherence times measured were $T_{2,C1}^* = 9.85 \pm 0.39$ ms for carbon-1 and $T_{2,C4}^* = 6.68 \pm 0.22$ ms for carbon-4. It should be noted that these T_2^* values are not limited by the electron coherence.

²This note will be removed: I want to make the statement about using this method to determine frequencies: Because the experiment extends for a long time the detuning to the precession frequency can be very accurately determined making this method also useful for determining frequencies.

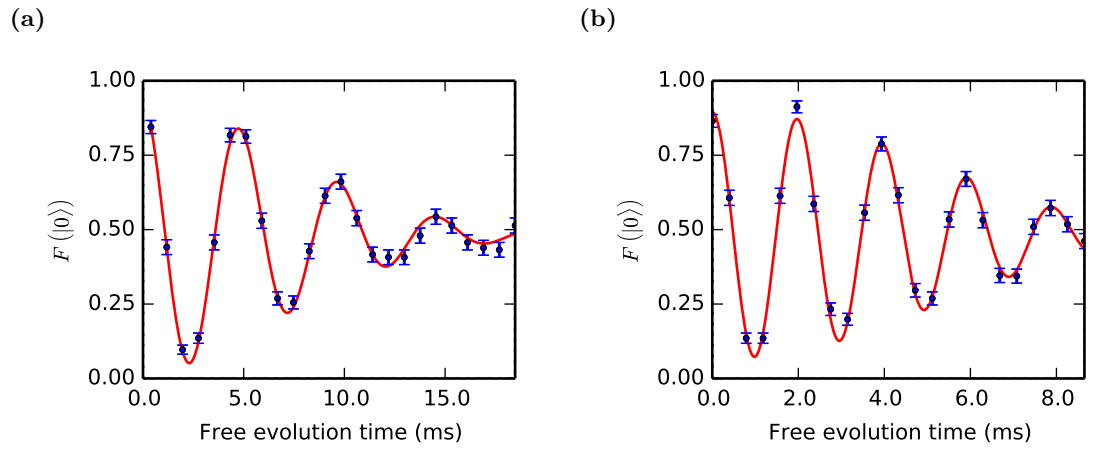


Figure 3.9 – Carbon-Ramsey experiment to determine T_2^* for nuclei while decoupling the electron. The decays are fitted with a generalized normal distribution to determine T_2^* and the exponent n . Figure 3.9a, for carbon-1, $T_{2,C1}^* = 9.85 \pm 0.39\text{ms}$ and $n = 1.83 \pm 0.19$. Figure 3.9b, for carbon-4, $T_{2,C4}^* = 6.68 \pm 0.22\text{ms}$ and $n = 2.31 \pm 0.31$.

4

Controlling Weakly-coupled Carbon Spins

The creation of entanglement is an essential capability for QEC in particular and quantum-computation in general. This chapter demonstrates how weakly coupled nuclear spins can be initialized and read-out and how this can be used to generate entanglement between them. The creation of entanglement is demonstrated with a quantum state tomography.

4.1 Initialization and readout of single spins

A weakly coupled spin can be initialized by conditionalizing on a readout result, similar to how nitrogen-MBI works. A weakly coupled carbon spin can be read-out by using the $\pm x$ -gate to entangle the phase of the electronic-spin with the state of the nuclear spin and reading out the phase of the electronic spin.

The gates used to initialize and readout a weakly coupled carbon are very similar. The gates used to initialize a weakly coupled carbon are depicted in Fig. 4.1. The circuit depicted in Fig. 4.1a projects the state along the the x -axis upon readout of the electronic spin. By adding an additional conditional gate, as depicted in Fig. 4.1b, the nuclear spin can be brought into the $|0\rangle$ -state regardless of the measurement outcome of the electronic spin.



Figure 4.1 – Figure 4.1a MBI-based initialization into $\pm|X\rangle$. Initializes the carbon into $|X\rangle_C$ when $|0\rangle_e$ is measured and into $|-X\rangle_C$ when $|1\rangle_e$ is measured for the electron. Figure 4.1b MBI-swap initialization into $|0\rangle$. Initializes the carbon into $|0\rangle_C$ regardless of the electronic spin-state measured.

To initialize the nuclear spin an initial pulse brings the electronic spin in $|X\rangle_e$. When the nuclear spin starts in the mixed state the system can be described by the tensor product of two density matrices:

$$\rho_X \otimes \rho_m = \rho_X \otimes \rho_X + \rho_X \otimes \rho_{-X} \quad (4.1)$$

By applying the $\pm x$ -gate the electronic-spin picks up a phase depending on the nuclear spin-state:

$$\rho_Y \otimes \rho_X + \rho_{-Y} \otimes \rho_{-X} \quad (4.2)$$

By reading out the electronic spin along the y -axis the nuclear spin is projected into the $|X\rangle_C$ or $|-X\rangle_C$ -state. This correlates the electronic-spin readout to the x -projection of the nuclear spin. By conditionalizing on a positive readout result the state can be initialized into the $|X\rangle_C$ -state. By applying an additional $\mp y$ gate on the nucleus it can be initialized into $|0\rangle$.

A weakly coupled carbon can be read out along the x -direction using the same circuit as used to initialize into $|X\rangle$. By changing the conditional gate to $\pm y$ the carbon can be read out along y . In order to read out the carbon along the z -direction an additional $\pm x$ -gate must be added before the initial y -pulse and the second conditional gate must be $\pm y$. It should be noted that the z -readout does not leave the nuclear spin in $|0\rangle$ or $|1\rangle$ but in $|Y\rangle$ or $|-Y\rangle$.

Figure 4.2 demonstrates initialization and readout. In Fig. 4.2a carbon-1 is initialized into the $|X\rangle_C$ -state and in Fig. 4.2b it is initialized into the $|0\rangle_C$ -state. This is done by implementing the circuits depicted in Fig. 4.1 and conditionalizing on a positive electron readout result.

The blue points correspond to x -readout, the green points to y -readout and the red points to z -readout. The phase is swept to demonstrate that the readouts function as intended. For a qubit in the $|0\rangle$ -state the initial phase is undefined.

The combined fidelity of readout and initialization to the desired state is: $F(|X\rangle) = 90.57 \pm 0.85\%$ for the $|X\rangle$ -state and $F(|Z\rangle) = 93.00 \pm 0.31\%$ for the $|Z\rangle$ -state.

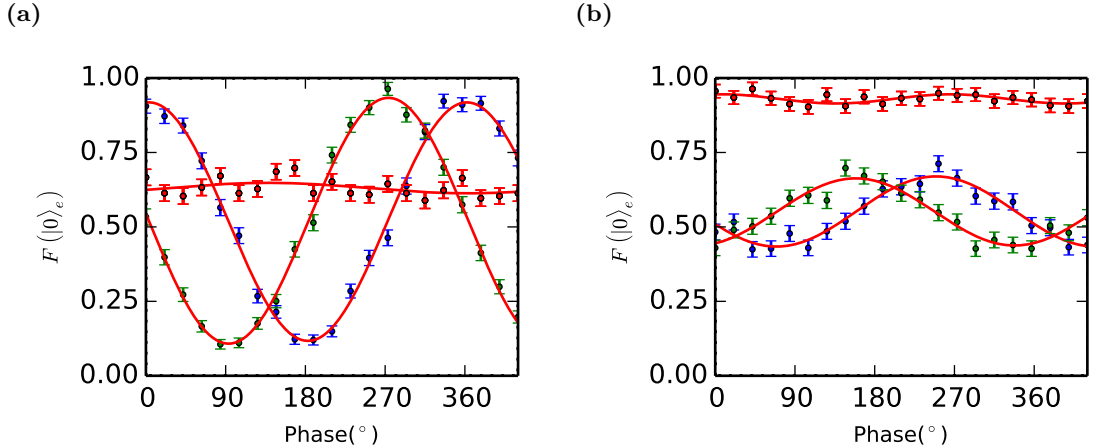


Figure 4.2 – Demonstration of carbon initialization and readout. In Fig. 4.2a carbon-1 is initialized in $|X\rangle$ and read-out. In Fig. 4.2b carbon-1 is initialized in $|0\rangle$. Colored points correspond to readouts in different bases, blue to x -readout, green to y -readout and red to z -readout.

4.2 The parity measurement

Entanglement between two qubits can be created by performing a parity measurement on them and conditionalizing on the outcome.

A parity measurement does not measure the state of two qubits but measures if two qubits are the same in a certain basis. An example is the XX-parity measurement. The XX-parity measurement returns a positive result if the two qubits are the same in the x -basis and a negative result if the two are opposite. That is it returns a positive result if the state is $|X, X\rangle$ or $|-, -\rangle$ and a negative result if the state is $|X, -\rangle$ or $|-, X\rangle$. In general a two qubit parity operator has 2 eigenvalues, both are twofold degenerate.

The XX-parity measurement can be implemented on a weakly coupled carbon spins using the circuit depicted in Fig. 4.3. A parity measurement is very similar to the regular readout depicted in Fig. 4.1a. Once the electron is brought into a superposition the electron picks up phase when the $\pm x$ -gate is applied. $+\pi/2$ -phase when the carbon is in $|+X\rangle$ and $-\pi/2$ -phase when the carbon is in $|-, -\rangle$. This is done for both carbons, when both carbons are in the same x -state the electron will pick up π -phase. When they do not give the same result the phase cancels. By reading out the electronic-spin along x the parity is measured. It should be noted that because we use a $\pm x$ -gate instead of a CNOT-gate an additional $\pi/2$ -phase is added to the carbon states compared to a regular parity measurement.

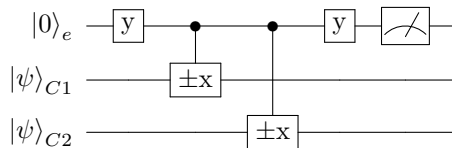


Figure 4.3 – Gate circuit for a XX-parity measurement.

4.3 Quantum state tomography

To demonstrate entanglement, entanglement must not only be created but it must also be verified that the entangled state is created. This can be done by performing a quantum state tomography. In a quantum state tomography the density matrix of a quantum state is reconstructed by repeatedly preparing the same state and gathering measurement statistics in different bases.

An arbitrary matrix can be described as a weighted sum of the Pauli-matrices and the Identity as in: Eq. (4.3).

$$\rho = I + \sum_{i,j} a_{i,j} \sigma_i \otimes \sigma_j \quad (4.3)$$

By measuring the coefficients of Eq. (4.3) the density matrix ρ can be reconstructed completely.

4.3.1 Readout

To measure the coefficients of Eq. (4.3) single and multi qubit measurements are needed. Single qubit measurements were described in Section 4.1. The two qubit measurements required are very similar to parity measurements but do not need to preserve the state after the measurement.

The parity measurement depicted in Fig. 4.3 can be used to measure the XX-parity. By changing the phase of one or two of the two $\pm x$ gates Y-parities can be measured. By applying a $\mp y$ to one of the two carbons before the initial Y-pulse a Z-parity can be measured, care must be taken however that the phase difference between this gate and the $\pm x$ on the corresponding carbon is 90° .

4.3.2 Initialization and tomography of multiple weakly coupled spins

The tomography is tested on two initialized two qubit states. The combined fidelity of the initialization and tomography is calculated by comparing to the ideal case.

Figure 4.4a shows a tomography of carbon-1 and carbon-4 initialized in the $|00\rangle$ -state. In the ideal case the single qubit Z-measurements and the ZZ parity are 1 and all other coefficients are 0. The ideal case is represented by the gray bars in the Fig. 4.4a. The fidelity to the ideal case is $F = 81.43 \pm 1.68\%$.

Figure 4.4b shows a tomography of carbon-1 and carbon-4 initialized in the $|01\rangle$ -state. In the ideal case ZI = 1 and IZ and ZZ are -1, all other coefficients are 0. The ideal case is represented by the gray bars in the Fig. 4.4b. The fidelity to the ideal case prediction is $80.99 \pm 1.69\%$.

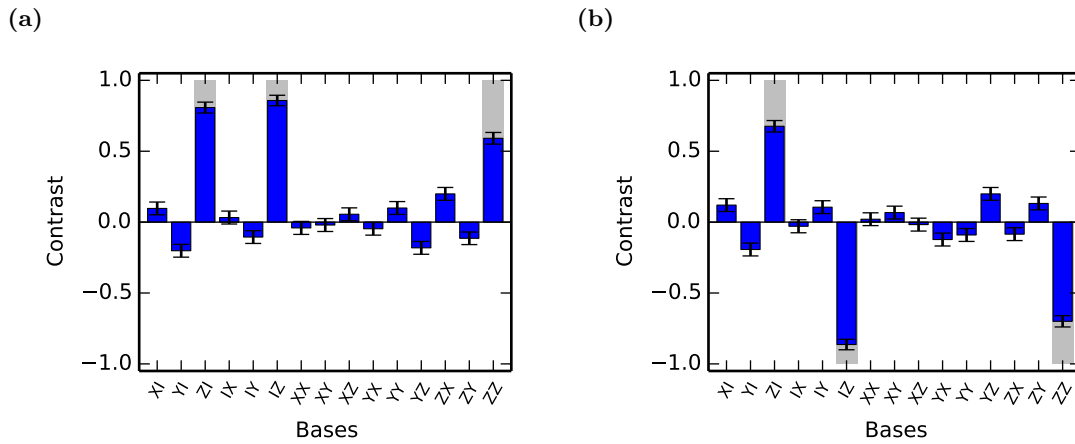


Figure 4.4 – Quantum state tomographies of two initialized carbons. In Fig. 4.4a the carbons are initialized into $|00\rangle$ with a fidelity of $81.43 \pm 1.68\%$. In Fig. 4.4b the carbons are initialized into $|10\rangle$ with a fidelity of $80.99 \pm 1.69\%$.

4.4 Demonstrating entanglement between weakly coupled carbons

By combining multi-qubit initialization, parity measurements and the quantum state tomography it is possible to demonstrate entanglement. After the qubits are initialized an XX-parity is performed

and the tomography is conditionalized on the negative readout result. The experiment is done for carbons initialized in $|00\rangle$ and carbons initialized in $|01\rangle$.

By conditionalizing on the negative readout result the carbons are projected into the negative-parity eigenstates of the XX-parity operator. These are $|{-X}, X\rangle$ and $|{-X}, X\rangle$. The tomography coefficient for the XX-parity is trivially -1. The other coefficients depend on the initial state the parity was performed on. The expected coefficients are again as gray bars.

Figure 4.5a shows the tomography for the negative XX parity of the $|00\rangle$ -state. $|00\rangle$ can be written in the X-basis as:

$$\frac{1}{2} (|X, X\rangle + |X, -X\rangle + |-X, X\rangle + |-X, -X\rangle) \quad (4.4)$$

By measuring the negative XX-parity the state is projected onto:

$$\Psi = \frac{1}{\sqrt{2}} (|X, -X\rangle + |-X, X\rangle) \quad (4.5)$$

In the yy -basis this state can be written as:

$$\Psi = \frac{1}{\sqrt{2}} (|Y, Y\rangle + |-Y, -Y\rangle) \quad (4.6)$$

And in the zz -basis this is:

$$\Psi = \frac{1}{\sqrt{2}} (|00\rangle - |11\rangle) \quad (4.7)$$

When measured in yy and zz this results in positive parity. The expectation for the ideal case is represented by the gray bars. The fidelity to the ideal case prediction is $76.60 \pm 1.74 \%$.

Figure 4.5b shows the tomography for the negative XX parity of the $|01\rangle$ -state. $|01\rangle$ can be written in the X-basis as:

$$\frac{1}{2} (|X, X\rangle - |X, -X\rangle + |-X, X\rangle - |-X, -X\rangle) \quad (4.8)$$

By measuring the negative XX-parity the state is projected onto:

$$\Phi = \frac{1}{\sqrt{2}} (|-X, X\rangle - |X, -X\rangle) \quad (4.9)$$

In the yy -basis this state can be written as:

$$\Phi = \frac{i}{\sqrt{2}} (|Y, -Y\rangle - |-Y, Y\rangle) \quad (4.10)$$

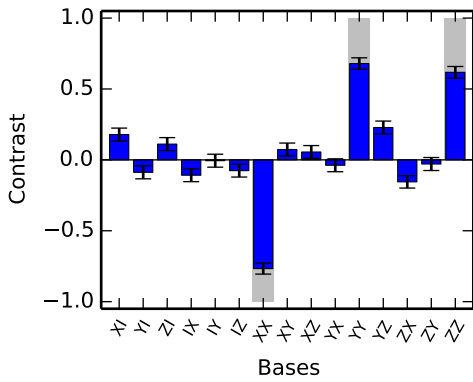
And in the zz -basis this is:

$$\Phi = \frac{1}{\sqrt{2}} (|10\rangle - |01\rangle) \quad (4.11)$$

When measured in yy and zz this results in negative parity. The expectation for the ideal case is represented by the gray bars. The fidelity to the ideal case prediction is $76.08 \pm 1.74 \%$

Both measured parities show a fidelity to the entangled state well above 0.5, clearly demonstrating that we have succeeded in creating an entangled state.

(a)



(b)

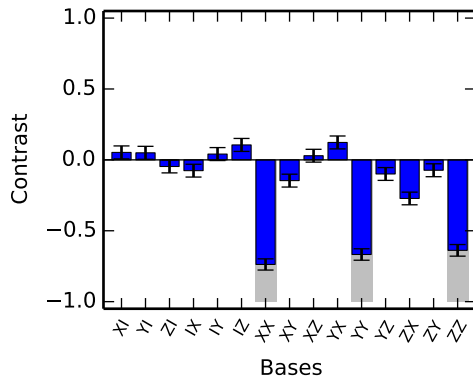


Figure 4.5 – Quantum state tomographies for entangled states created by measuring a negative XX parity. Figure 4.5a is the negative XX-parity of the state prepared in Fig. 4.4a. It is in the $\frac{1}{\sqrt{2}}(|X, -X\rangle + |X, -X\rangle)$ with $76.60 \pm 1.74\%$ fidelity. Figure 4.5b is the negative XX-parity of the state prepared in Fig. 4.4b. It is in the $\frac{1}{\sqrt{2}}(|X, -X\rangle - |X, -X\rangle)$ with $76.08 \pm 1.74\%$ fidelity.

5

Outlook: towards Quantum Error Correction

This thesis has demonstrated the probabilistic creation of entangled states between weakly-coupled carbon spins. This chapter will provide an outlook on how the tools developed can be used to implement quantum error correction. It will also discuss the feasibility of using weakly-coupled carbon spins as a means to enlarge NV-spin registers in general

5.1 Direct outlook, deterministic operations/what needs to be done/can be done

5.2 Simulations, how many carbon can we control?

Moved from identification section:

5.2.1 Effect of the magnetic field

There are significant advantages to increasing the magnetic field when attempting to address weakly coupled carbons. By increasing the magnetic field the Larmor frequency can be increased, reducing the number of carbons that are in the complex regime. This causes the broad oscillating resonances to disappear allowing more carbons to be addressed.

Although increasing the magnetic field can improve the situation it is not always possible or desired. When the magnetic field becomes too strong too strong the resonances become narrower than the resolution of the Arbitrary Waveform Generator used to generate the pulses that address the resonances, making it impossible to address these resonances effectively. Simulations were performed (see ??) that indicate that for a natural carbon-13 concentration there is a range between 400G and 1400G where the magnetic field is optimal for controlling weakly coupled spins.

Besides the spin environment there are other factors affecting the choice for magnetic field. Because the optical transitions used for readout and initialization depend on strain and magnetic field field[10], care must be taken when measuring that states do not mix in the excited state. This combined with the fact that few experiments have been performed at high magnetic field and low temperature make it more practical to settle for a more moderate magnetic field of 300G.

Idem:

Spins that have a stronger than average hyperfine-interaction show up outside or at the edge of the spin-bath collapse. Spins that are in the basic regime show up as a narrow dip. Going to larger τ separates these dips further as the order of the resonance k increases. By looking at larger τ it is possible to resolve and address more resonances. Several spins in the basic regime have been identified 3 of these are visible as colored lines in Fig. 3.3. As computations are fundamentally limited by the coherence time there is a limit to the resonance-order that can be used to address carbons, making it impossible to resolve all weakly coupled spins.

Besides the carbons in the basic regime there are also weakly-coupled carbons that are more strongly coupled. When a carbon in the complex regime is present in the NV-center this manifests itself as a resonance with strong oscillations on the side. Such a feature is also clearly visible in Fig. 3.3. We have identified the oscillations in the fingerprint as belong to a single spin which is denoted by the red line.

When a weakly coupled carbon in the complex regime is present a significant part of the fingerprint spectrum is inaccessible for controlling other carbons making them an undesired feature when attempting to control weakly coupled carbon spins.

Bibliography

- [1] N Bar-Gill, L M Pham, A Jarmola, D Budker, and R L Walsworth. Solid-state electronic spin coherence time approaching one second. *Nature communications*, 4:1743, 1 2013. ISSN 2041-1723. URL <http://www.ncbi.nlm.nih.gov/pubmed/23612284>.
- [2] H. Bernien. *Control, Measurement and Entanglement of Remote Quantum Spin Registers in Diamond*. PhD thesis, Delft University of Technology, 2014.
- [3] L. Childress and R. Hanson. Diamond nv centers for quantum computing and quantum networks. *MRS Bulletin*, 38(02):134–138, 2 2013. ISSN 0883-7694. URL http://www.journals.cambridge.org/abstract_S0883769413000201.
- [4] G. de Lange. *Quantum Control and Coherence of Interacting Spins in Diamond*. PhD thesis, Delft University of Technology, 2012.
- [5] G. de Lange, Z.H. Wang, D. Rist, V.V. Dobrovitski, and R. Hanson. Universal dynamical decoupling of a single solid-state spin from a spin bath. *Science (New York, N.Y.)*, 330(6000):60–3, 10 2010. ISSN 1095-9203. URL <http://www.ncbi.nlm.nih.gov/pubmed/20829452>.
- [6] Marcus W. Doherty, Neil B. Manson, Paul Delaney, Fedor Jelezko, Jrg Wrachtrup, and Lloyd C.L. Hollenberg. The nitrogen-vacancy colour centre in diamond. *Physics Reports*, 528(1):1–45, 7 2013. ISSN 03701573. URL <http://linkinghub.elsevier.com/retrieve/pii/S0370157313000562>.
- [7] Richard P. Feynman. Simulating physics with computers. *International Journal of Theoretical Physics*, 21(6-7):467–488, 6 1982. ISSN 0020-7748. URL <http://link.springer.com/10.1007/BF02650179>.
- [8] Adam Gali. Identification of individual isotopes of nitrogen-vacancy center in diamond by combining the polarization studies of nuclear spins and first-principles calculations. *Physical Review B*, 80(24):241204, 12 2009. ISSN 1098-0121. URL <http://link.aps.org/doi/10.1103/PhysRevB.80.241204>.
- [9] Adam Gali, Maria Fyta, and Efthimios Kaxiras. Ab initio supercell calculations on nitrogen-vacancy center in diamond: Electronic structure and hyperfine tensors. *Physical Review B*, 77(15):155206, 4 2008. ISSN 1098-0121. URL <http://link.aps.org/doi/10.1103/PhysRevB.77.155206>.
- [10] Bas Jorrit Hensen. *Measurement-based Quantum Computation with the Nitrogen-Vacancy centre in Diamond*. PhD thesis, Delft University of Technology, 2011.
- [11] F. Jelezko, T. Gaebel, I. Popa, a. Gruber, and J. Wrachtrup. Observation of coherent oscillations in a single electron spin. *Physical Review Letters*, 92(7):076401, 2 2004. ISSN 0031-9007. URL <http://link.aps.org/doi/10.1103/PhysRevLett.92.076401>.
- [12] L. Robledo, L. Childress, H. Bernien, B. Hensen, P.F.A. Alkemade, and R. Hanson. High-fidelity projective read-out of a solid-state spin quantum register. *Nature*, 477(7366):574–8, 9 2011. ISSN 1476-4687. URL <http://www.ncbi.nlm.nih.gov/pubmed/21937989>.

- [13] P.W. Shor. Algorithms for quantum computation: discrete logarithms and factoring. In *Proceedings 35th Annual Symposium on Foundations of Computer Science*, pages 124–134. IEEE Comput. Soc. Press, 1994. ISBN 0-8186-6580-7. URL <http://ieeexplore.ieee.org/lpdocs/epic03/wrapper.htm?arnumber=365700>.
- [14] Benjamin Smeltzer, Lilian Childress, and Adam Gali. 13 c hyperfine interactions in the nitrogen-vacancy centre in diamond. *New Journal of Physics*, 13(2):025021, 2 2011. ISSN 1367-2630. URL <http://stacks.iop.org/1367-2630/13/i=2/a=025021?key=crossref.bdd6956722cde89a36ab3eee44a82724>.
- [15] T. H. Taminiau, J. J. T. Wagenaar, T. van der Sar, F. Jelezko, V. V. Dobrovitski, and R. Hanson. Detection and control of individual nuclear spins using a weakly coupled electron spin. *Physical Review Letters*, 109(13):137602, 9 2012. ISSN 0031-9007. URL <http://link.aps.org/doi/10.1103/PhysRevLett.109.137602>.
- [16] T. H. Taminiau, J.J.T. J. T. Wagenaar, T. van der Sar, F. Jelezko, V.V. V. Dobrovitski, and R. Hanson. Detection and control of individual nuclear spins using a weakly coupled electron spin. *Physical Review Letters*, 109(13):137602, 9 2012. ISSN 0031-9007. URL <http://link.aps.org/doi/10.1103/PhysRevLett.109.137602><http://arxiv.org/abs/1205.4128>.
- [17] T. H. TH Taminiau, J. Cramer, T. van der Sar, V. V. Dobrovitski, and R. Hanson. Universal control and error correction in multi-qubit spin registers in diamond. *Nature Nanotechnology*, 2(February):2–7, 9 2014. ISSN 1748-3387. URL <http://arxiv.org/abs/1309.5452><http://www.nature.com/doifinder/10.1038/nnano.2014.2>.
- [18] T. van der Sar, Z.H. Wang, M.S. Blok, H. Bernien, T.H. Taminiau, D.M. Toyli, D.A. Lidar, D.D. Awschalom, R. Hanson, and V.V. Dobrovitski. Decoherence-protected quantum gates for a hybrid solid-state spin register. *Nature*, 484(7392):82–6, 4 2012. ISSN 1476-4687. URL <http://www.ncbi.nlm.nih.gov/pubmed/22481361>.
- [19] L M Vandersypen, Matthias Steffen, Gregory Breyta, Costantino S Yannoni, Mark H Sherwood, and Isaac L Chuang. Experimental realization of shor’s quantum factoring algorithm using nuclear magnetic resonance. *Nature*, 414(6866):883–7, 2001. ISSN 0028-0836. URL <http://www.ncbi.nlm.nih.gov/pubmed/11780055>.

A

Dynamical Decoupling Spectroscopy

A.1 Mathematical description of dynamical decoupling spectroscopy

The response of a single carbon to a dynamical decoupling spectroscopy experiment is given by Eqs. (A.1) to (A.4) [16]. Where P_x is the probability that the initial spin-state is preserved and M_j the contrast.

$$P_x = (M + 1)/2 \quad (\text{A.1})$$

$$M_j = 1 - (1 - \hat{\mathbf{n}}_0 \cdot \hat{\mathbf{n}}_1) \sin^2 \frac{N\phi}{2} \quad (\text{A.2})$$

$$1 - \hat{\mathbf{n}}_0 \cdot \hat{\mathbf{n}}_1 = \frac{A_\perp^2}{\tilde{\omega}^2} \frac{(1 - \cos(\tilde{\omega}\tau))(1 - \cos(\omega_L\tau))}{1 + \cos(\tilde{\omega}\tau)\cos(\omega_L\tau) - (\frac{A_\parallel + \omega_L}{\tilde{\omega}}) \sin(\tilde{\omega}\tau)\sin(\omega_L\tau)} \quad (\text{A.3})$$

$$\phi = \cos^{-1} \left(\cos(\tilde{\omega}\tau)\cos(\omega_L\tau) - \left(\frac{A_\parallel + \omega_L}{\tilde{\omega}} \right) \sin(\tilde{\omega}\tau)\sin(\omega_L\tau) \right) \quad (\text{A.4})$$

The contrast of an ensemble of spins in a dynamical decoupling spectroscopy M is given by the product of all individual values M_j for each individual spin j (Eq. (A.5)).

$$M = \prod_j M_j \quad (\text{A.5})$$

A.2 Fingerprint analysis

The estimated hyperfine parameters of all 13 identified spins can be found in Table A.1. Due to the size of the fingerprint analysis it is not possible to include with this thesis. A pdf file containing the fingerprint analysis can be found here: <https://www.dropbox.com/s/gieji9e86bfvsf1/fingerprinting.pdf>.

Carbon	A_{\parallel}	A_{\perp}
1	$2\pi \cdot 30.0$ kHz	$2\pi \cdot 80.0$ kHz
2	$2\pi \cdot 27.0$ kHz	$2\pi \cdot 28.5$ kHz
3	$2\pi \cdot -51.0$ kHz	$2\pi \cdot 105.0$ kHz
4	$2\pi \cdot 45.1$ kHz	$2\pi \cdot 20.0$ kHz
5	$2\pi \cdot 17.0$ kHz	$2\pi \cdot 10.0$ kHz
6	$2\pi \cdot -15.0$ kHz	$2\pi \cdot 12.0$ kHz
7	$2\pi \cdot -23.0$ kHz	$2\pi \cdot 12.0$ kHz
8	$2\pi \cdot 10.0$ kHz	$2\pi \cdot 8.0$ kHz
9	$2\pi \cdot 8.0$ kHz	$2\pi \cdot 12.0$ kHz
10	$2\pi \cdot -9.3$ kHz	$2\pi \cdot 13.0$ kHz
11	$2\pi \cdot -10.0$ kHz	$2\pi \cdot 5.0$ kHz
12	$2\pi \cdot -30.0$ kHz	$2\pi \cdot 35.0$ kHz
13	$2\pi \cdot -32.0$ kHz	$2\pi \cdot 20.0$ kHz

Table A.1 – Estimated hyperfine parameters for spins 1 to 13.

B

Constants and Experimental values

Constants	
μ_0	$4\pi \cdot 10^{-7} \frac{\text{V}\cdot\text{s}}{\text{A}\cdot\text{m}}$
Gyromagnetic Ratios	
γ_e	$2\pi \cdot 2.8025 \text{ MHz/G}$
γ_N	$2\pi \cdot 0.3077 \text{ kHz/G}$
γ_C	$2\pi \cdot 1.0705 \text{ kHz/G}$
Interaction Strengths	
Δ	$2\pi \cdot 2.878 \text{ GHz}$
Q	$2\pi \cdot 4.946 \text{ MHz}$
A_N	$2\pi \cdot 2.186 \text{ MHz}$
Optics	
637 nm	471 THz

Acknowledgements